

Monitoring Shelf Sea Dynamics with Ocean-Bottom Distributed Acoustic Sensing

Loïc Viens¹, Zack Jack Spica², Brent G. Delbridge¹, and Brian K. Arbic³

¹Los Alamos National Laboratory

²University of Michigan

³University of Michigan-Ann Arbor

March 16, 2023

Abstract

The mixing of ocean waters on continental shelves, which is mainly driven by waves, tides, and currents, plays a key role in the physics, biogeochemistry, and ecology of coastal regions. This study focuses on four months of continuous data recorded along a telecommunication cable offshore Oregon, USA, with Distributed Acoustic Sensing (DAS). We apply a cross-correlation approach to the continuous DAS data to infer the propagation of ocean surface gravity waves in the 3 to 100 s period range and estimate near-surface ocean flows. We observe strong spatio-temporal variations of ocean flows along the cable over four months, with strong impacts from a series of storms in late October 2021. We find that our measurements capture oceanic surface motions as those measured by nearby traditional oceanographic instruments. This study demonstrates that ocean-bottom DAS can be used to infer the dynamic properties of near-shore oceans with an unprecedented spatio-temporal resolution.

1 **Monitoring Shelf Sea Dynamics with Ocean-Bottom**
2 **Distributed Acoustic Sensing**

3 **Loïc Viens¹, Zack J. Spica², Brent G. Delbridge¹, and Brian K. Arbic²**

4 ¹Los Alamos National Laboratory, Los Alamos, New Mexico, USA

5 ²Department of Earth and Environmental Sciences, University of Michigan, Ann Arbor, Michigan, USA

6 **Key Points:**

- 7 • Ocean-Bottom Distributed Acoustic Sensing (OBDAS) is used to infer the prop-
8 agation of ocean surface gravity waves (OSGWs) and ocean flows
9 • Four months of OBDAS data recorded offshore Oregon reveal modulations of OS-
10 GWs by bathymetry, tides, swell events, and storms
11 • The inferred ocean flows from OBDAS data agree well with coincident measure-
12 ments from buoys and high-frequency radars

Corresponding author: Loïc Viens, lviens@lanl.gov

Abstract

The mixing of ocean waters on continental shelves, which is mainly driven by waves, tides, and currents, plays a key role in the physics, biogeochemistry, and ecology of coastal regions. This study focuses on four months of continuous data recorded along a telecommunication cable offshore Oregon, USA, with Distributed Acoustic Sensing (DAS). We apply a cross-correlation approach to the continuous DAS data to infer the propagation of ocean surface gravity waves in the 3 to 100 s period range and estimate near-surface ocean flows. We observe strong spatio-temporal variations of ocean flows along the cable over four months, with strong impacts from a series of storms in late October 2021. We find that our measurements capture oceanic surface motions as those measured by nearby traditional oceanographic instruments. This study demonstrates that ocean-bottom DAS can be used to infer the dynamic properties of near-shore oceans with an unprecedented spatio-temporal resolution.

Plain Language Summary

Continental shelves are highly active drivers affecting the ocean's biology due to the ocean mixing driven by waves, tides, and currents. This study focuses on monitoring the ocean flow offshore the coast of Oregon, USA, using Distributed Acoustic Sensing (DAS). DAS is a technology that repurposes fiber-optic cables into arrays of thousands of vibration sensors. We probed 55 km of an ocean-bottom telecommunication cable to measure continuous Earth's vibrations every 20 m over four months. The propagation of landward and oceanward ocean surface gravity waves in the 3 to 100 s period range is inferred from the DAS data and used to estimate the ocean flow along the cable. We observe strong spatio-temporal variations of the near-surface flow, which correlate well with observed ocean physical properties made by external measurements, such as moored buoys and high-frequency radars. The high density of DAS measurements allows us to better understand the ocean flow with a high spatio-temporal resolution, which is not attainable with traditional oceanographic instruments.

1 Introduction

Shelf seas, which refer to ocean waters on continental shelves, are important drivers of biogeochemical ocean activity and have been recognized as highly productive zones (Longhurst et al., 1995). The mixing of these shallow and nutrient-rich ocean waters is driven by a complex set of physical mechanisms including tides, wind waves, swell, currents, internal waves, and wind-forced up/down-welling. Physical models (e.g., Parker, 2007), which predict ocean currents and wave height, are critical to mitigate daily water-related hazards for mariners and to study and control local public health threats, such as harmful algal blooms and oil spills. However, the resolution of existing models is too coarse to accurately predict sudden, infrequent, and significant variations caused by punctual events such as storms, explosive cyclogenesis (i.e., weather bombs), and meteotsunamis (Benetazzo et al., 2013). These transient and small-scale variations pose a significant hazard to populations living in coastal regions, and new observational techniques are needed to monitor the dynamics of shelf seas.

Offshore the coast of the State of Oregon, USA, the width of the continental shelf extends between 17 and 74 km from the coastline with typical maximum water depths of ~ 150 m. In this region, surface currents have been studied with traditional ocean monitoring instruments, including moored buoys and current meters (Kundu & Allen, 1976; Richards, 1981), acoustic Doppler current profilers (Barth et al., 2000), and onshore high-frequency radars (Kosro, 2005). These existing methods reveal that tides, wind-driven currents, and up/down-welling events are significant contributors to the ocean circulation off the west coast of the United States (Castelao & Barth, 2005). However, the sparse distribution of these measurements is insufficient to capture the full dynamics and spa-

63 tial extent of surface currents. This study overcomes this limitation by deriving high spatio-
64 temporal resolution observations of ocean flow using acoustic tomography methods ap-
65 plied to Ocean Bottom Distributed Acoustic Sensing (OBDAS) measurements.

66 Classical ocean acoustic tomography uses active acoustic sources and receivers to
67 measure acoustic wave travel times and infer ocean properties such as currents and tem-
68 perature (e.g. W. Munk & Wunsch, 1979). However, the relatively complex installation
69 of underwater acoustic source/receiver sensors combined with the potential impact on
70 marine life limits active ocean tomography applications. To overcome these drawbacks,
71 passive ocean acoustic tomography methods have also been developed (Brown et al., 2014;
72 Godin et al., 2010; Godin, G Brown, et al., 2014). Passive tomography is based on the
73 retrieval of an approximation of the Green’s function (i.e., wave propagation) between
74 two sensors by cross-correlating their continuous records (Lobkis & Weaver, 2001). In
75 a moving fluid medium, measurements of acoustic nonreciprocity, which is defined as the
76 difference between the sound propagation in opposite directions between the two sen-
77 sors, can be used to determine the direction and speed of the fluid motion. This method
78 was extended to ocean surface gravity waves (OSGWs) and infra-gravity waves recorded
79 by buoys (Brown & Lu, 2016) and seafloor pressure gauges (Godin, Zabotin, et al., 2014;
80 Neale et al., 2015; Tonegawa et al., 2018; Harmon et al., 2012). Recently, OBDAS has
81 also been demonstrated to capture the pressure perturbations on the seafloor caused by
82 the propagation of OSGWs, and has been used to monitor ocean near-surface currents
83 (Williams et al., 2022).

84 The Distributed Acoustic Sensing (DAS) technology uses an interrogator unit (IU)
85 to probe fiber-optic cables and measure the vibrations (i.e., strain or strain rate) of the
86 Earth over tens of kilometers with a high spatio-temporal resolution (every $\sim 1\text{--}50$ m at
87 $\sim 100\text{--}1000$ Hz depending on the experimental setting, Hartog, 2017). Over the past few
88 years, DAS experiments have probed underwater telecommunication cables and recorded
89 a variety of physical signals including near-coast microseisms (Guerin et al., 2022; Xiao
90 et al., 2022; Spica et al., 2020; Viens, Pertou, et al., 2022), local, regional and teleseis-
91 mic earthquakes (Lior et al., 2021; Shinohara et al., 2019; Spica et al., 2022; Viens, Bonilla,
92 et al., 2022), T-phases and other acoustic waves (Rivet et al., 2021; Ugalde et al., 2021;
93 Spica et al., 2022), and ocean surface gravity waves (OSGWs) and deep-ocean water mix-
94 ing processes (Mata Flores et al., 2022; Ide et al., 2021; Lindsey et al., 2019; Sladen et
95 al., 2019; Williams et al., 2019, 2022). Most of these datasets are relatively short, span-
96 ning from a few days to a few weeks, and therefore do not capture the ocean’s seasonal
97 dynamics.

98 Using four months of continuous OBDAS data recorded offshore the coast of Ore-
99 gon, we infer the propagation of OSGWs in the 0.01–0.3 Hz frequency band (i.e., 3–100
100 s) and the resulting ocean near-surface flow. Wind waves, which are generated by a lo-
101 cal transfer of energy from the wind to the ocean surface, are generally present at the
102 higher end of the frequency spectrum (>0.1 Hz). At frequencies below 0.1 Hz, the swell,
103 which is excited by wind waves from distant storms, dominates the spectrum and dis-
104 plays dispersive frequency features. Both wind waves and swell interact with coastal bathymetry
105 and are refracted and reflected as they approach the coastline. The shoaling and break-
106 ing process of OSGWs can also generate infragravity (typically, 0.004–0.04 Hz) waves
107 which reflect off the coast and propagate oceanward (W. H. Munk, 1949; Janssen et al.,
108 2003; Sheremet et al., 2002).

109 We first introduce the datasets used in this study and present a cross-correlation
110 approach used to infer the propagation of OSGWs and estimate near-surface ocean flows
111 from OBDAS data. We then present our results and compare them with more traditional
112 ocean measurements obtained in the region of interest. We finally discuss the different
113 physical phenomena captured by our analysis and the potential of OBDAS to probe the
114 water column with an unprecedented spatio-temporal resolution.

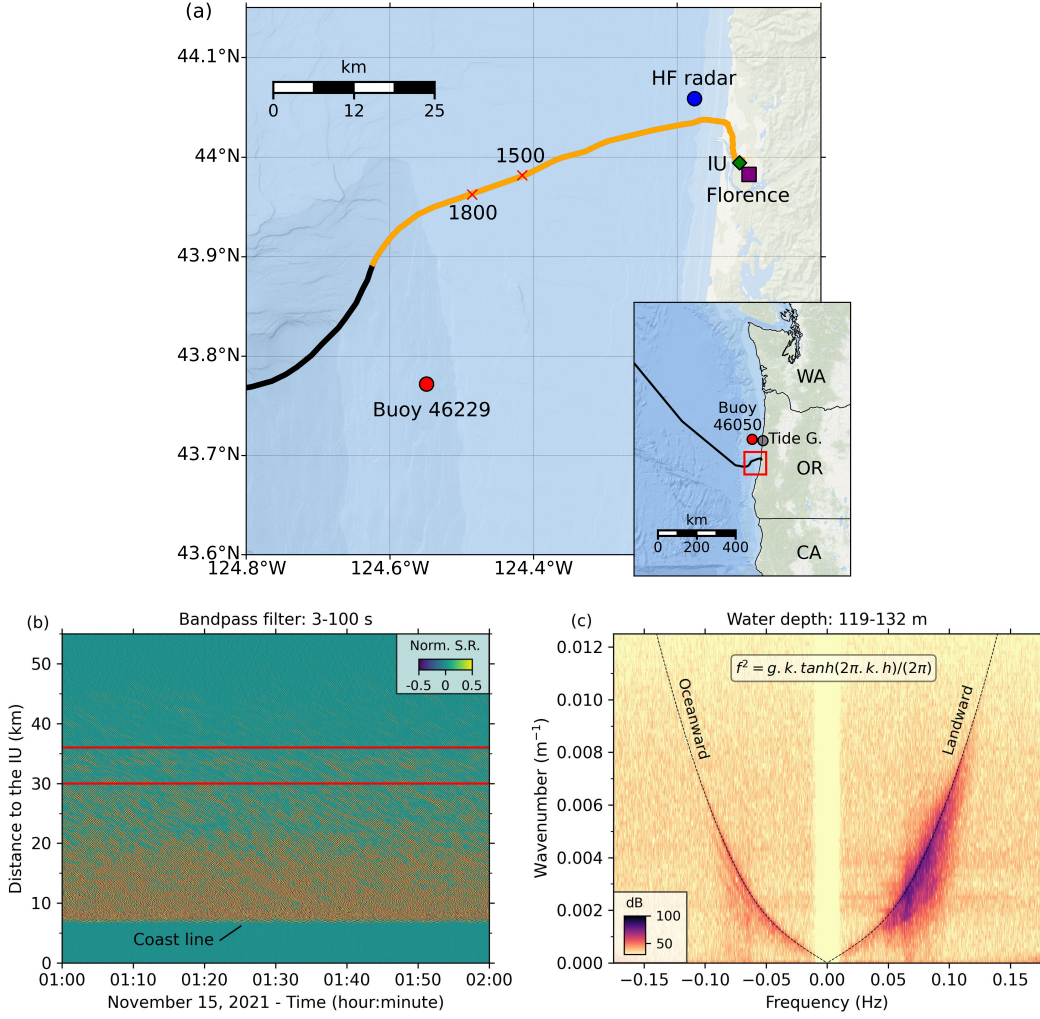


Figure 1. (a) Bathymetry map offshore Florence, Oregon, including the path of the AKORN telecommunication cable (orange and black line). The orange section of the cable is probed in this study from the IU (green diamond) and the location of channels 1500 and 1800 are highlighted. The positions of NDBC buoy 46229 and high-frequency radar surface current measurements are shown by the red and blue circles, respectively. The inset map shows the west coast of the United States, the AKORN cable (black), the zoomed region near Florence (red square), and the locations of NDBC buoy 46050 (red circle) and a tide gauge (grey circle). (b) One hour of amplitude normalized strain-rate data bandpass filtered between 3 and 100 s recorded on November 15, 2021 along the cable. The two red lines highlight the region over which the frequency-wavenumber ($f-k$) analysis shown in (c) is performed (i.e., between channels 1500 and 1800). (c) $f-k$ spectrum of the waves shown in (b) between the two red lines. The OSGW theoretical dispersion curves using a water depth (h) of 126 m are shown by the dashed lines.

2 Data

2.1 DAS data

A FEBUS Optics A1-R IU was used to probe the first 55 km of the Alaska-Oregon Network (AKORN) telecommunication cable from Florence, Oregon, between August 6 and December 1, 2021 (Figure 1a). The IU recorded strain-rate data with a channel spacing of 20 m, a gauge length of 40 m, and a 100 Hz sampling rate. The data are continuous except for a 3-day gap between September 7–10. According to the cable installation report, the first 6.3 km of the cable link the landing station to the coastline through a series of pipes located along roads. The following 49 km of the probed section are buried offshore under 80–100 cm of sediments. Between 6.3 and 40 km from the IU, the cable is on the continental shelf with a water depth of less than ~ 150 m. The bathymetry then drops from 150 to 300 m between 40 and 55 km from the IU as the cable reaches the edge of the continental shelf. From the coastline, the average azimuth of the offshore cable is $\sim 254^\circ$ from the north. This angle is close to the $\sim 275^\circ$ angle from the north, representing the direction perpendicular to the mean shoreline direction given its $\sim 5^\circ$ azimuth from the north.

The continuous strain-rate data are downsampled to 10 Hz and filtered between 3 and 100 s using a two-pass four-pole Butterworth bandpass filter. An example one-hour DAS strain-rate time series recorded along the cable is shown in Figure 1b. Both landward and oceanward propagating waves with apparent velocities slowing down as they approach the coastline can be observed in the time domain. To illustrate the characteristics of the recorded waves, we examine a frequency-wavenumber (f - k) spectrum of the time series calculated between 30 and 36 km from the IU (Figure 1c). The landward and oceanward waves generally follow the OSGW dispersion relationship $f^2 = g.k \tanh(2\pi.k.h)/(2\pi)$, where f is the frequency, g is the gravitational acceleration, k is the wavenumber, and h is the water depth (i.e., 127 m, Mei et al., 2018). A similar behavior is observed all along the cable, which indicates that the DAS strain-rate measurements are dominated by OSGWs in the 3 to 100 s period range. The landward propagating waves are expected to be more energetic than the oceanward propagating waves due to dissipation associated with the wave breaking in the surf zone (Miche, 1951; Elgar et al., 1994), and correspondingly we observe that the landward waves have higher energy levels in the f - k domain. Moreover, the landward energy spreads over a broader frequency range than the theoretical relationship. This is likely caused by the fact that OSGWs cross the cable at slightly oblique angles leading to higher apparent velocities and a smaller apparent wavenumber at such distances from the coastline (Williams et al., 2022). Nevertheless, landward OSGWs are likely refracted by the decreasing bathymetry as they approach the coastline, and their propagation should eventually yield a direction nearly perpendicularly to the coastline (i.e., almost along the cable axis).

2.2 Buoy, high-frequency radar, and tide gauge data

The National Data Buoy Center (NDBC) of the National Oceanic and Atmospheric Administration (NOAA) develops, operates, and maintains a network of buoys and coastal stations (Evans et al., 2003). To validate the DAS results, we download the continuous data (e.g., wave height and direction as well as wind speed and direction) recorded at two buoys (Figure 1). Buoy 46229 is the closest to the cable (water depth: 180 m), but a maintenance event prevented the data from being collected for over a month during the DAS experiment. Therefore, we also analyze the continuous data collected at buoy 46050 (water depth: 160 m), which recorded similar data due to comparable water depths (Figure S1).

The NDBC also distributes data from U.S. high-frequency radars through the Integrated Ocean Observing System (IOOS) Program (Harlan et al., 2010). We analyze hourly measurements of the east-west ocean surface current (i.e., top 2.4 m of the ocean)

166 at one coastal location near the cable (Figure 1a). The east-west data are obtained from
 167 the radial component of the surface current at several high-frequency radars, and have
 168 a horizontal resolution of 6 km (Kim et al., 2008).

169 Tide gauges managed by NOAA have been measuring water levels along U.S coast-
 170 lines for more than a century. We finally collect the data from a tide gauge (Station ID:
 171 9435380), located in South Beach, Oregon, ~ 75 km north of the cable (Figure 1a).

172 **3 Methods: OSGW propagation and ocean flow measurements**

173 To determine the spatio-temporal evolution of OSGWs, we select the strain-rate
 174 time series recorded offshore (i.e., between channels 300 and 2500) and divide the con-
 175 tinuous waveforms into 10-min time windows. We apply a f - k filter to the 10-min time
 176 series to separate the landward and oceanward propagating OSGWs (Figure S2), and
 177 further select waves propagating within the velocity range we expect to observe the OS-
 178 GWs (2-50 m/s) to exclude signals such as seismic and acoustic waves traveling at higher
 179 velocities. The signals are then transformed back to the time domain, demeaned, and
 180 detrended. We apply 1-bit normalization to the time series (Bensen et al., 2007), which
 181 involves setting the positive and negative signals to 1 and -1, respectively, to improve
 182 the retrieval of the signal's phase information. For both landward and oceanward prop-
 183 agating OSGWs, cross-correlation functions (CCFs) are computed for each 10-minute
 184 pre-processed time window by considering every 5 channels as virtual sources and the
 185 15th channel before each virtual source as receivers (e.g., receiver channel 1485 for vir-
 186 tual source 1500; see Text S2 and Figure S2 for more details about the CCF computa-
 187 tion). To increase the signal-to-noise ratio of the CCFs, we stack the 10-min CCFs over
 188 four hours (i.e., stack 24 CCFs) using a phase-weighted stack approach (power: 2, smooth-
 189 ing: 0.5 s; Schimmel & Paulssen, 1997) with a two-hour overlap. Figures 2a-b show an
 190 example of the waveforms between channels 1500 and 1485. Both landward and ocean-
 191 ward CCFs display clear phase arrivals varying through time, but landward propagat-
 192 ing OSGWs exhibit stronger variations.

193 The apparent velocity of the near-surface flow can be obtained by measuring the
 194 wave travel time difference between the landward and oceanward propagating OSGWs
 195 (Godin, G Brown, et al., 2014). We use a stretching method (Sens-Schönfelder & We-
 196 gler, 2006) to estimate the relative travel time changes (dt/t) between landward and ocean-
 197 ward propagating waves. We stretch/compress 100 s of each four-hour landward CCF
 198 starting at 10 s, and find the stretching value that best fits the corresponding oceanward
 199 propagating OSGW. The stretching is performed with a grid search algorithm in two steps;
 200 we first use ten values uniformly distributed between -25 and 25% of stretching to find
 201 an initial guess of the stretching coefficient, and then refine the measurement by inter-
 202 polating the stretched waveforms 250 times between the neighboring values. The best
 203 match is found using a correlation coefficient (CC) with values between 0 and 1. A value
 204 of 1 indicates a perfect match between the landward and oceanward CCFs after stretch-
 205 ing. To ensure the reliability of the dt/t measurements, we only analyze the results where
 206 the CCs after stretching are higher than 0.4 (i.e., 94.4% of the dt/t values; Figure S3).

207 We show an example of the measured relative travel time changes (dt/t) for the CCFs
 208 computed between channels 1500 and 1485 in Figure 2c. For this station pair, the CCs
 209 after stretching between the landward and oceanward propagating OSGWs have a mean
 210 value of 0.85, which demonstrates a high similarity between the waveforms. The aver-
 211 age dt/t value over the four months of data in Figure 2c is 0.04 s, which indicates a gen-
 212 eral landward ocean near-surface flow. Moreover, clear dt/t temporal variations can be
 213 observed through time, such as a strong landward flow between October 1 and 10, 2021,
 214 as well as numerous short periods of time with oceanward flows.

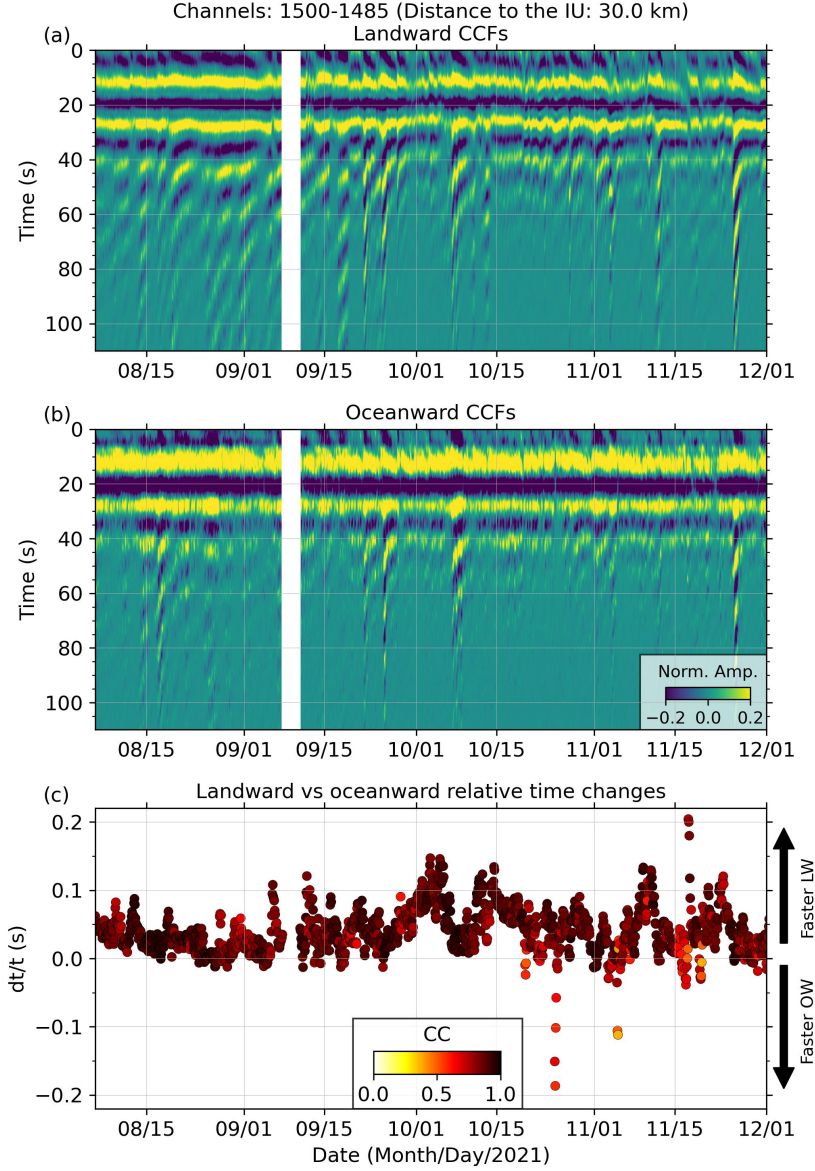


Figure 2. (a) Causal (positive) part of the amplitude normalized CCFs computed between virtual source 1500 and receiver 1485, which captures the landward (LW) propagation of OS-GWs. The amplitude is clipped for visibility. (b) Anti-causal (negative) part of the amplitude normalized CCFs computed between the same channels, which represents the oceanward (OW) propagation of OSGWs. (c) Relative travel time changes (dt/t) between the landward and oceanward propagating waves, which represent the ocean near-surface flow. Positive and negative dt/t values indicate that the ocean flow is faster landward and oceanward, respectively. The color of each data point represents the CC after stretching between the landward and oceanward propagating waves.

4 Results and discussion

We repeat the dt/t measurements for all the virtual source-receiver pairs along the cable and show the results in Figure 3a and the corresponding CCs after stretching in Figure S3. Over the four months of data, we observe clear spatio-temporal variations of the ocean near-surface flow along the cable.

To focus on the spatial variations of the ocean near-surface flow, we average the dt/t measurements over the four months of data for each station pair (Figure 4a). Bathymetry changes (retrieved from NOAA National Geophysical Data Center, 2008, Figures 3b and 4a) can significantly impact the propagation of OSGWs, and likely cause some of the spatial variations of the ocean flow. The regions between 12 and 20 km from the IU and on the edge of the continental shelf (i.e., after 45 km), where relatively large bathymetry changes happen over short distances, are mainly dominated by an oceanward flow. In contrast, between 20 and 45 km from the IU, where the bathymetry is relatively flat with an average slope of less than 0.5% (Figure S4), landward flow is observed. The coastal region (6.3 to 12 km from the IU), which exhibits large and shallow bathymetry changes, displays a mix of landward and oceanward flows.

Shoaling and refraction of OSGWs happen when the waves become sensitive to the ocean bottom, typically at water depths (h) of less than about half of the OSGW wavelength ($h < 0.5\lambda$). We estimate potential shoaling effects at 16.9 and 47.5 km from the IU, where oceanward flows highlighted by average dt/t values of -0.04 s are observed. The water depths at these two locations are 79 and 206 m, and should impact OSGWs with wavelengths of 158 and 412 m which corresponds to wavenumbers of 0.0063 and 0.0024 m^{-1} , respectively (Figure 4a). To relate these theoretical wavenumbers to the DAS measurements, we compute time-averaged f - k spectra around 16.9 and 47.5 km from the IU (Figure S5). The theoretical wavenumbers are close to the highest energy levels of the f - k spectra for wind waves (> 0.1 Hz) and swell (< 0.1 Hz) at 16.9 and 47.5 km from the IU, respectively. This indicates that the oceanward flow observed in these two regions is likely caused by a velocity decrease of the incoming swell on the edge of the continental shelf and wind waves closer to the coast. This velocity reduction may also be coupled with an increase of the oceanward OSGW velocity due to the increasing water depth. In addition to shoaling effects, incoming OSGWs can also be reflected towards the ocean by bathymetry changes and generate oceanward near-surface flows (Sheremet et al., 2002; Ardhuin et al., 2003; Ardhuin & Roland, 2012), and oceanward propagating infragravity waves can contribute to the observed oceanward flows (Sheremet et al., 2002; Neale et al., 2015). However, the relatively broad frequency content of the CCFs does not allow us to fully understand the driving mechanism of such spatial variations, and future work should be performed to fully characterize the ocean flow.

To better understand the temporal variations of the ocean near-surface flow, we also show the wave height time series recorded at NDBC buoys 46229 and 46050 in Figure 3a. The dt/t variations measured at distances between 43 to 46 km from the interrogator, where the height of the water column is similar to that at the buoys (i.e., ~ 160 m), are generally in phase with the buoy wave height changes. Time periods with higher and lower wave heights correlate with landward and oceanward near-surface flows, respectively.

In Figure 3c, we decompose the total wave height recorded at buoy 46050 into wind wave and swell wave height components by summing the information at frequencies higher and smaller than 0.1 Hz, respectively. During swell events, we generally observe stronger landward ocean flows (i.e., positive dt/t values) from the coast to ~ 40 km from the IU (Figure 3a) and stronger oceanward flows on the edge of the continental shelf (i.e., after 45 km from the IU), which indicates that swell events impact the dynamics of the entire shelf sea. The observed temporal variations in the flows are likely caused by the

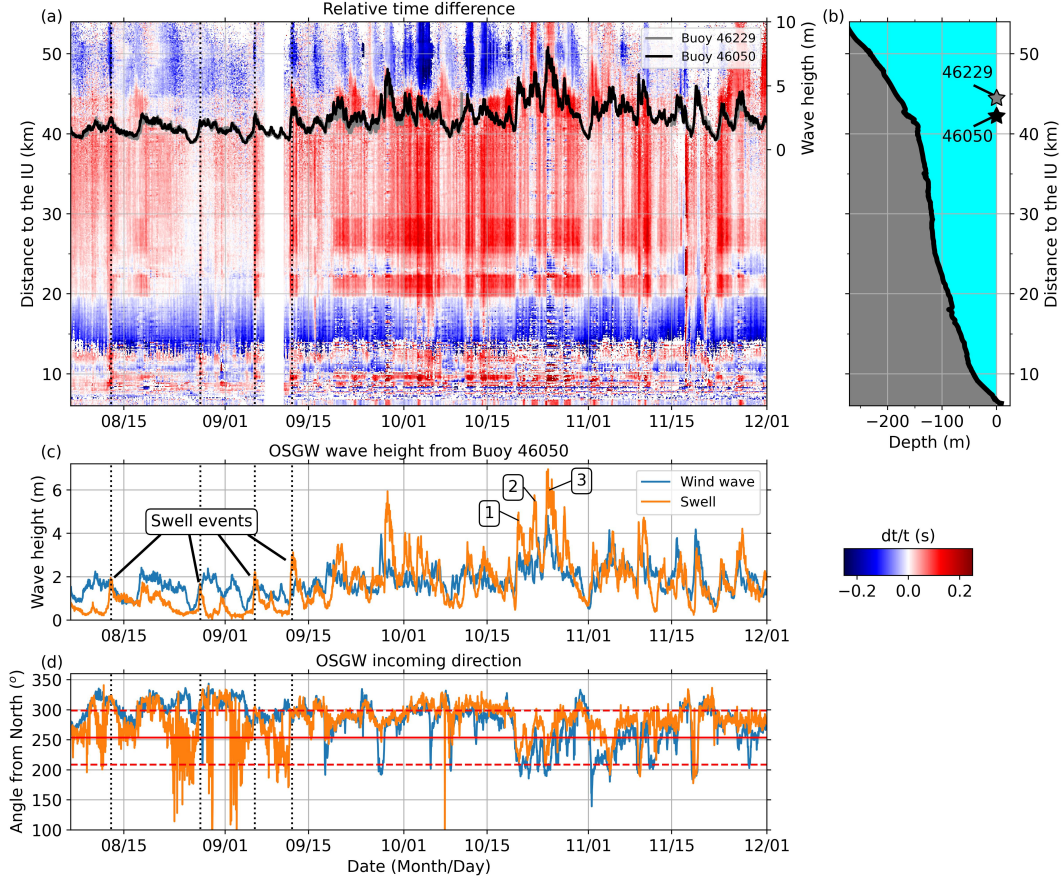


Figure 3. (a) Relative travel time changes (dt/t) between landward and oceanward propagating OSGWs along the cable over the four months of data. The dt/t data with a CC after stretching less than 0.4 are set to zero (white areas). The grey and black lines are the wave height recorded at NDBC buoys 46229 and 46050, respectively. The vertical dotted lines highlight the examples of swell events shown in (c). (b) Bathymetry profile along the cable including the location of the two buoys if they were to be along the cable. (c) OSGW (blue) and swell (orange) wave heights from buoy 46050. Examples of swell events are highlighted and their timing are indicated by the vertical dotted lines. The three storms that passed in the vicinity of the Pacific Northwest in late October 2021 are identified by numbers, with the weather bomb being the third storm. (d) OSGW (blue) and swell (orange) wave directions from buoy 46050. The solid and dashed red lines represent the azimuth of the cable (254° from the north) and the $\pm 45^{\circ}$ angles, respectively

266 low-frequency content and low wavenumber of swell events, which are sensitive to the
267 water depth variations on the edge of the continental shelf.

268 The direction of propagation of OSGWs impacts the dt/t measurements, with larger
269 propagation angles relative to the direction of the cable resulting in faster apparent ve-
270 locities (Figures 3d-4b). Substantial variations of the OSGW propagation direction are
271 observed through time, with a clear change of the general direction of propagation of swell
272 and wind waves after October 20, 2021 (Figure 3d). This change coincides with a gen-
273 eral shift of the wind direction in the region of interest (Figure S6). Overall, we calcu-
274 late that the swell and wind waves travel within a $\pm 45^\circ$ angle from the axis of the ca-
275 ble during 68% and 61% of the time, respectively.

276 To further analyze the effect of the direction of propagation of OSGWs on the dt/t
277 results, we show the dt/t values for the CCFs computed between channels 2300 and 2285
278 along with the wave height at buoy 46050 from October 1 to November 30, 2021 in Fig-
279 ure 4b. We focus on this specific time period as a series of three storms passed in the
280 vicinity of the Pacific Northwest (Figure 3c). The third storm evolved into an explosive
281 cyclogenesis on October 24 and generated wave heights up to 8 m at buoy 46050 (Fig-
282 ure 4b). The wave height variations are generally well matched by the dt/t measurements
283 during and after the passing of the three storms, but clear differences can be observed
284 in early/mid-October (Figure 4b). The difference between the incoming angle of the OS-
285 GWs and the axis of the cable is also shown in Figure 4b. When OSGWs travel within
286 a $\pm 45^\circ$ angle from the cable, a good agreement between the dt/t measurements and the
287 wave height measured at the buoy is observed. For larger propagation angles, there is
288 a clear discrepancy between the two types of measurements. As only the apparent ve-
289 locity of the near-surface flow is measured with DAS, larger apparent surface flows are
290 expected during time periods when ocean surface waves do not travel along the axis of
291 the cable. Future studies could investigate the potential of combining both types of in-
292 struments to compute a transfer function of dt/t measurements to wave height by con-
293 sidering the ocean wave direction.

294 Incoming OSGWs are refracted as they reach shallower water, which should result
295 in a propagation direction that tends to be along the axis of the cable nearshore. In Fig-
296 ure 4c, we compare the dt/t values computed between channels 390 and 375 with east-
297 west ocean surface current measurements from high-frequency radars. Over the 1.5 months
298 of data, we generally observe similar long-term variations of the ocean flow with the two
299 types of measurements. Daily variations of the high-frequency radar surface currents,
300 which are primarily driven by tides (Figure S7), are also matched by the dt/t measure-
301 ments. However, some differences can be observed and can be explained by three phe-
302 nomena. First, high-frequency radar only captures the surface current over the first 2.4
303 m of the ocean. The exact sampling depth of the dt/t measurements is unknown due to
304 the large period range used in this study, but is likely deeper than that of the radar mea-
305 surements. Second, the high-frequency radar measurements are centered 2 km north of
306 channel 390 (Figure 1a) and are averaged over a 6 by 6 km horizontal grid, which is dif-
307 ferent from OBDAS measurements between two channels located 300 m apart. Finally,
308 while OSGWs are expected to travel almost along the axis of the cable, we cannot ex-
309 clude deviations of the angle of incoming OSGWs that would impact the dt/t measure-
310 ments.

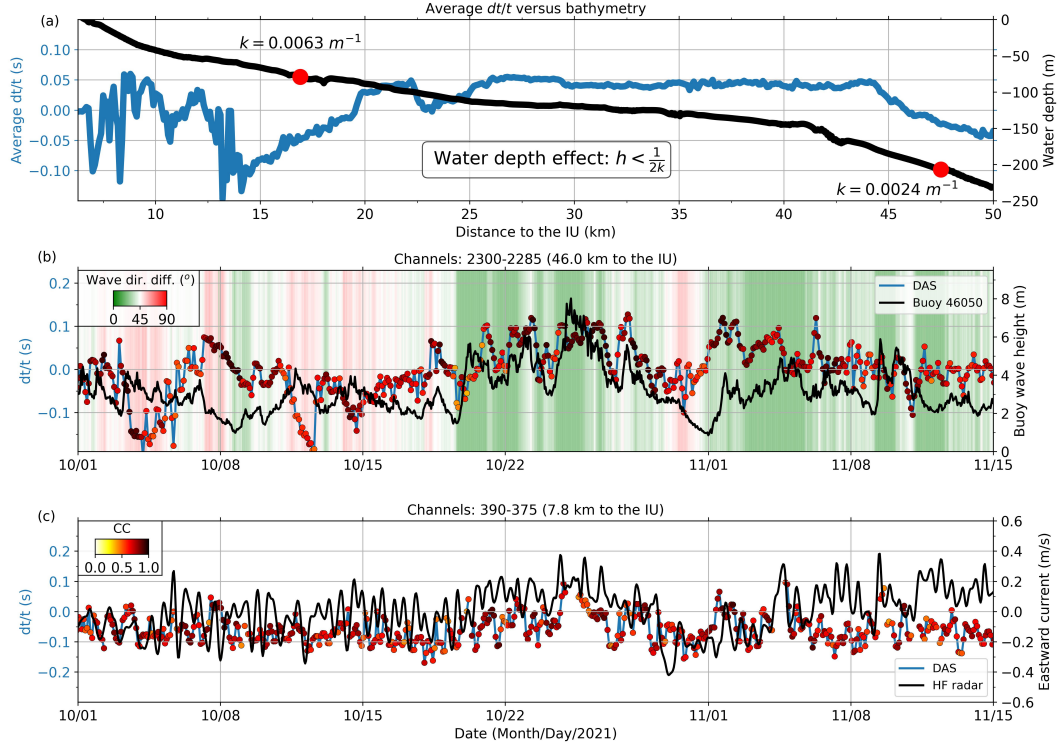


Figure 4. (a) Average dt/t values (blue) over four months for each channel pair along the cable. The bathymetry profile is shown in black. The wavenumbers at which OSGWs are theoretically affected by the ocean bottom at two locations are also indicated. (b) Comparison between relative time changes (dt/t) obtained from DAS channels located approximately where the ocean depth is 160 m (colored dots and blue line) and buoy 46050 wave height measurements (black). The background color corresponds to the absolute difference between the average wave direction between 0.05 and 0.5 Hz and the direction of the cable. Angles of zero and 90 degrees correspond to waves traveling parallel and perpendicular to the cable, respectively. (c) Relative travel time changes (dt/t) versus eastward surface currents obtained by high-frequency radar at a location near channel 390.

5 Conclusions

We demonstrated that OBDAS can be used to monitor shelf sea dynamics by analyzing four months of continuous strain-rate data recorded offshore the coast of Oregon. The DAS data are used to infer the propagation of landward and ocean OSGWs and estimate near-surface ocean flows, which are shown to be modulated by tides, swell events, and storms. The extent of the cable over 49 km from the coast also allowed us to characterize the effect of bathymetry changes on the ocean-surface flow as OSGWs are impacted by strong bathymetry changes. We finally observed a good correlation between the ocean flow measured with OBDAS and those obtained with external measurements, especially when OSGWs propagate along the axis of the cable.

Our measurements demonstrate the potential of OBDAS to investigate the dynamics of near-surface flows with an unprecedented spatio-temporal resolution. Such measurements of the water column could potentially be critical for a variety of offshore applications, including rapid tsunami early warning after large subduction earthquakes and to improve energy production from wave turbines.

6 Open Research

The archiving of the data and codes developed to perform the technical analysis and to reproduce the figures is underway and pending LANL approval. The data and codes will be made publicly available on GitHub-Zenodo upon completion of LANL internal review.

Acknowledgments

L.V. was partially supported by NSF award EAR2022716 and is currently supported by the Chick Keller Fellowship from the Center for Space and Earth Science (CSES) at Los Alamos National Laboratory (LANL). CSES is funded by LANL's Laboratory Directed Research and Development (LDRD) program under project number 20210528CR. Z.J.S. acknowledges support from the Air Force Research Laboratory grant FA9453-21-2-0018. We thank Alaska Communication for providing access to its subsea fiber infrastructure, and are grateful to the NOAA for providing buoy and coastal station data. The manuscript has a Los Alamos National Laboratory Unlimited Release Number (LA-UR-23-22290).

Competing interests: The authors declare that they have no competing interests.

References

- Ardhuin, F., O'Reilly, W. C., Herbers, T. H. C., & Jessen, P. F. (2003). Swell transformation across the continental shelf. part i: Attenuation and directional broadening. *Journal of Physical Oceanography*, *33*(9), 1921 - 1939. Retrieved from https://journals.ametsoc.org/view/journals/phoc/33/9/1520-0485_2003_033_1921_statcs_2.0.co_2.xml doi: 10.1175/1520-0485(2003)033<1921:STATCS>2.0.CO;2
- Ardhuin, F., & Roland, A. (2012). Coastal wave reflection, directional spread, and seismoacoustic noise sources. *Journal of Geophysical Research: Oceans*, *117*(C11). Retrieved from <https://agupubs.onlinelibrary.wiley.com/doi/abs/10.1029/2011JC007832> doi: <https://doi.org/10.1029/2011JC007832>
- Barth, J. A., Pierce, S. D., & Smith, R. L. (2000). A separating coastal upwelling jet at cape blanco, oregon and its connection to the california current system. *Deep Sea Research Part II: Topical Studies in Oceanography*, *47*(5), 783-810. Retrieved from <https://www.sciencedirect.com/science/article/pii/S0967064599001277> doi: [https://doi.org/10.1016/S0967-0645\(99\)00127-7](https://doi.org/10.1016/S0967-0645(99)00127-7)
- Benetazzo, A., Carniel, S., Sclavo, M., & Bergamasco, A. (2013). Wave-current interaction: Effect on the wave field in a semi-enclosed basin. *Ocean Modelling*, *70*, 152-165. Retrieved from <https://www.sciencedirect.com/science/article/pii/S1463500312001862> (Ocean Surface Waves) doi: <https://doi.org/10.1016/j.ocemod.2012.12.009>
- Bensen, G. D., Ritzwoller, M. H., Barmin, M. P., Levshin, A. L., Lin, F., Moschetti, M. P., ... Yang, Y. (2007). Processing seismic ambient noise data to obtain reliable broad-band surface wave dispersion measurements. *Geophys. J. Int.*, *169*, 1239-1260. doi: 10.1111/j.1365-246X.2007.03374.x
- Brown, M. G., Godin, O. A., Williams, N. J., Zabotin, N. A., Zabolina, L., & Banker, G. J. (2014). Acoustic green's function extraction from ambient noise in a coastal ocean environment. *Geophys. Res. Lett.*, *41*(15), 5555-5562. Retrieved from <https://agupubs.onlinelibrary.wiley.com/doi/abs/10.1002/2014GL060926> doi: <https://doi.org/10.1002/2014GL060926>
- Brown, M. G., & Lu, C. (2016). Green's function retrieval in a field of random water waves. *Wave Motion*, *60*, 8-19. Retrieved from <https://www.sciencedirect.com/science/article/pii/S0165212515001171> doi: <https://doi.org/10.1016/j.wavemoti.2015.08.003>
- Castelao, R. M., & Barth, J. A. (2005). Coastal ocean response to summer upwelling favorable winds in a region of alongshore bottom topography variations

- 377 off oregon. *Journal of Geophysical Research: Oceans*, 110(C10). Retrieved
 378 from [https://agupubs.onlinelibrary.wiley.com/doi/abs/10.1029/](https://agupubs.onlinelibrary.wiley.com/doi/abs/10.1029/2004JC002409)
 379 [2004JC002409](https://doi.org/10.1029/2004JC002409) doi: <https://doi.org/10.1029/2004JC002409>
- 380 Elgar, S., Herbers, T. H. C., & Guza, R. T. (1994). Reflection of ocean surface
 381 gravity waves from a natural beach. *Journal of Physical Oceanography*,
 382 24(7), 1503 - 1511. Retrieved from [https://journals.ametsoc.org/view/](https://journals.ametsoc.org/view/journals/phoc/24/7/1520-0485_1994_024_1503_roosgw_2_0_co_2.xml)
 383 [journals/phoc/24/7/1520-0485_1994_024_1503_roosgw_2_0_co_2.xml](https://journals/ametsoc.org/view/journals/phoc/24/7/1520-0485_1994_024_1503_roosgw_2_0_co_2.xml) doi:
 384 [10.1175/1520-0485\(1994\)024<1503:ROOSGW>2.0.CO;2](https://doi.org/10.1175/1520-0485(1994)024<1503:ROOSGW>2.0.CO;2)
- 385 Evans, D., Conrad, C. L., & Paul, F. M. (2003). *Handbook of automated data qual-*
 386 *ity control checks and procedures of the national data buoy center* (Tech. Rep.
 387 Nos. Document 03-02). NOAA National Data Buoy Center Tech.
- 388 Godin, O. A., G Brown, M., Zabolin, N. A., Zabolina, L. Y., & Williams, N. J.
 389 (2014). Passive acoustic measurement of flow velocity in the straits of florida.
 390 *Geoscience Letters*, 1(1), 16. Retrieved from [https://doi.org/10.1186/](https://doi.org/10.1186/s40562-014-0016-6)
 391 [s40562-014-0016-6](https://doi.org/10.1186/s40562-014-0016-6) doi: [10.1186/s40562-014-0016-6](https://doi.org/10.1186/s40562-014-0016-6)
- 392 Godin, O. A., Zabolin, N. A., & Goncharov, V. V. (2010). Ocean tomography with
 393 acoustic daylight. *Geophys. Res. Lett.*, 37(13). Retrieved from [https://](https://agupubs.onlinelibrary.wiley.com/doi/abs/10.1029/2010GL043623)
 394 agupubs.onlinelibrary.wiley.com/doi/abs/10.1029/2010GL043623 doi:
 395 <https://doi.org/10.1029/2010GL043623>
- 396 Godin, O. A., Zabolin, N. A., Sheehan, A. F., & Collins, J. A. (2014). Interfer-
 397 ometry of infragravity waves off new zealand. *Journal of Geophysical Research:*
 398 *Oceans*, 119(2), 1103-1122. Retrieved from [https://agupubs.onlinelibrary](https://agupubs.onlinelibrary.wiley.com/doi/abs/10.1002/2013JC009395)
 399 [.wiley.com/doi/abs/10.1002/2013JC009395](https://doi.org/10.1002/2013JC009395) doi: [https://doi.org/10.1002/](https://doi.org/10.1002/2013JC009395)
 400 [2013JC009395](https://doi.org/10.1002/2013JC009395)
- 401 Guerin, G., Rivet, D., van den Ende, M. P. A., Stutzmann, E., Sladen, A., & Am-
 402 puero, J.-P. (2022). Quantifying microseismic noise generation from coastal
 403 reflection of gravity waves recorded by seafloor DAS. *Geophys. J. Int.*, 231(1),
 404 394-407. Retrieved from <https://doi.org/10.1093/gji/ggac200> doi:
 405 [10.1093/gji/ggac200](https://doi.org/10.1093/gji/ggac200)
- 406 Harlan, J., Terrill, E., Hazard, L., Keen, C., Barrick, D., Whelan, C., ... Kohut,
 407 J. (2010). The integrated ocean observing system high-frequency radar net-
 408 work: Status and local, regional, and national applications. *Marine Technology*
 409 *Society Journal*, 44(6), 122-132. doi: [doi:10.4031/MTSJ.44.6.6](https://doi.org/10.4031/MTSJ.44.6.6)
- 410 Harmon, N., Henstock, T., Srokosz, M., Tilmann, F., Rietbrock, A., & Barton,
 411 P. (2012). Infragravity wave source regions determined from ambient
 412 noise correlation. *Geophys. Res. Lett.*, 39(4). Retrieved from [https://](https://agupubs.onlinelibrary.wiley.com/doi/abs/10.1029/2011GL050414)
 413 agupubs.onlinelibrary.wiley.com/doi/abs/10.1029/2011GL050414 doi:
 414 <https://doi.org/10.1029/2011GL050414>
- 415 Hartog, A. (2017). *An introduction to distributed optical fibre sensors*. CRC Press.
 416 doi: <https://doi.org/10.1201/9781315119014>
- 417 Ide, S., Araki, E., & Matsumoto, H. (2021). Very broadband strain-rate measure-
 418 ments along a submarine fiber-optic cable off cape muroto, nankai subduction
 419 zone, japan. *Earth, Planets and Space*, 73(1), 1-10.
- 420 Janssen, T. T., Battjes, J. A., & van Dongeren, A. R. (2003). Long waves
 421 induced by short-wave groups over a sloping bottom. *Journal of Geo-*
 422 *physical Research: Oceans*, 108(C8). Retrieved from [https://agupubs](https://agupubs.onlinelibrary.wiley.com/doi/abs/10.1029/2002JC001515)
 423 [.onlinelibrary.wiley.com/doi/abs/10.1029/2002JC001515](https://doi.org/10.1029/2002JC001515) doi:
 424 <https://doi.org/10.1029/2002JC001515>
- 425 Kim, S. Y., Terrill, E. J., & Cornuelle, B. D. (2008). Mapping surface currents from
 426 hf radar radial velocity measurements using optimal interpolation. *Journal of*
 427 *Geophysical Research: Oceans*, 113(C10). Retrieved from [https://agupubs](https://agupubs.onlinelibrary.wiley.com/doi/abs/10.1029/2007JC004244)
 428 [.onlinelibrary.wiley.com/doi/abs/10.1029/2007JC004244](https://doi.org/10.1029/2007JC004244) doi: [https://](https://doi.org/10.1029/2007JC004244)
 429 doi.org/10.1029/2007JC004244
- 430 Kosro, P. M. (2005). On the spatial structure of coastal circulation off newport,
 431 oregon, during spring and summer 2001 in a region of varying shelf width.

- 432 *Journal of Geophysical Research: Oceans*, 110(C10). Retrieved from [https://](https://agupubs.onlinelibrary.wiley.com/doi/abs/10.1029/2004JC002769)
 433 agupubs.onlinelibrary.wiley.com/doi/abs/10.1029/2004JC002769 doi:
 434 <https://doi.org/10.1029/2004JC002769>
- 435 Kundu, P. K., & Allen, J. S. (1976). Some three-dimensional characteristics of
 436 low-frequency current fluctuations near the Oregon coast. *Journal of Physical*
 437 *Oceanography*, 6(2), 181 - 199. Retrieved from [https://journals.ametsoc](https://journals.ametsoc.org/view/journals/phoc/6/2/1520-0485_1976_006_0181_stdcol_2_0_co_2.xml)
 438 [.org/view/journals/phoc/6/2/1520-0485_1976_006_0181_stdcol_2_0_co_2](https://journals.ametsoc.org/view/journals/phoc/6/2/1520-0485_1976_006_0181_stdcol_2_0_co_2.xml)
 439 [.xml](https://journals.ametsoc.org/view/journals/phoc/6/2/1520-0485_1976_006_0181_stdcol_2_0_co_2.xml) doi: 10.1175/1520-0485(1976)006<0181:STDCOL>2.0.CO;2
- 440 Lindsey, N. J., Dawe, T. C., & Ajo-Franklin, J. B. (2019). Illuminating seafloor
 441 faults and ocean dynamics with dark fiber distributed acoustic sensing. *Sci-*
 442 *ence*, 366(6469), 1103–1107.
- 443 Lior, I., Sladen, A., Rivet, D., Ampuero, J.-P., Hello, Y., Becerril, C., ... Chris-
 444 tolos, M. (2021). On the Detection Capabilities of Underwater Distributed
 445 Acoustic Sensing. *Journal of Geophysical Research: Solid Earth*, 126(3),
 446 e2020JB020925. doi: 10.1029/2020JB020925
- 447 Lobkis, O. I., & Weaver, R. L. (2001). On the emergence of the Green's function
 448 in the correlations of a diffuse field. *The Journal of the Acoustical Society of*
 449 *America*, 110(6), 3011–3017. doi: 10.1121/1.1417528
- 450 Longhurst, A., Sathyendranath, S., Platt, T., & Caverhill, C. (1995). An estimate of
 451 global primary production in the ocean from satellite radiometer data. *Journal*
 452 *of Plankton Research*, 17(6), 1245-1271. Retrieved from [https://doi.org/10](https://doi.org/10.1093/plankt/17.6.1245)
 453 [.1093/plankt/17.6.1245](https://doi.org/10.1093/plankt/17.6.1245) doi: 10.1093/plankt/17.6.1245
- 454 Mata Flores, D., Sladen, A., Ampuero, J.-P., Mercerat, E. D., & Rivet, D. (2022).
 455 Monitoring deep sea currents with seafloor distributed acoustic sensing. *Sub-*
 456 *mitted to JGR - Oceans*.
- 457 Mei, C. C., Stiassnie, M. A., & Yue, D. K.-P. (2018). *Theory and applications of*
 458 *ocean surface waves* (3rd ed.). World Scientific. Retrieved from [https://www](https://www.worldscientific.com/doi/abs/10.1142/10212)
 459 [.worldscientific.com/doi/abs/10.1142/10212](https://www.worldscientific.com/doi/abs/10.1142/10212) doi: 10.1142/10212
- 460 Miche, M. (1951). Le pouvoir reflechissant des ouvrages maritimes exposes a l'action
 461 de la houle. *Annales de Ponts et Chaussées*, 121, 285-319. Retrieved from
 462 <https://cir.nii.ac.jp/crid/1573668924778624768>
- 463 Munk, W., & Wunsch, C. (1979). Ocean acoustic tomography: a scheme for large
 464 scale monitoring. *Deep Sea Research Part A. Oceanographic Research Papers*,
 465 26(2), 123-161. Retrieved from [https://www.sciencedirect.com/science/](https://www.sciencedirect.com/science/article/pii/0198014979900736)
 466 [article/pii/0198014979900736](https://www.sciencedirect.com/science/article/pii/0198014979900736) doi: [https://doi.org/10.1016/0198-0149\(79\)](https://doi.org/10.1016/0198-0149(79)90073-6)
 467 [90073-6](https://doi.org/10.1016/0198-0149(79)90073-6)
- 468 Munk, W. H. (1949). Surf beats. *Eos, Transactions American Geophysical Union*,
 469 30(6), 849-854. Retrieved from [https://agupubs.onlinelibrary.wiley](https://agupubs.onlinelibrary.wiley.com/doi/abs/10.1029/TR030i006p00849)
 470 [.com/doi/abs/10.1029/TR030i006p00849](https://agupubs.onlinelibrary.wiley.com/doi/abs/10.1029/TR030i006p00849) doi: [https://doi.org/10.1029/](https://doi.org/10.1029/TR030i006p00849)
 471 [TR030i006p00849](https://doi.org/10.1029/TR030i006p00849)
- 472 Neale, J., Harmon, N., & Srokosz, M. (2015). Source regions and reflection of
 473 infragravity waves offshore of the U.S. Pacific Northwest. *Journal of Geo-*
 474 *physical Research: Oceans*, 120(9), 6474-6491. Retrieved from [https://](https://agupubs.onlinelibrary.wiley.com/doi/abs/10.1002/2015JC010891)
 475 agupubs.onlinelibrary.wiley.com/doi/abs/10.1002/2015JC010891 doi:
 476 <https://doi.org/10.1002/2015JC010891>
- 477 NOAA National Geophysical Data Center. (2008). *Central Oregon coastal digi-*
 478 *tal elevation model*. Retrieved from [https://www.ncei.noaa.gov/access/](https://www.ncei.noaa.gov/access/metadata/landing-page/bin/iso?id=gov.noaa.ngdc.mgg.dem:11500)
 479 [metadata/landing-page/bin/iso?id=gov.noaa.ngdc.mgg.dem:11500](https://www.ncei.noaa.gov/access/metadata/landing-page/bin/iso?id=gov.noaa.ngdc.mgg.dem:11500)
- 480 Parker, B. (2007). *Tidal analysis and prediction, NOAA special publication nos co-*
 481 *ops 3* (Tech. Rep.). U.S. Department of Commerce, National Oceanic and At-
 482 mospheric Administration.
- 483 Richards, F. A. (Ed.). (1981). *Coastal upwelling* (Vol. 1). Washington, D. C.: AGU.
- 484 Rivet, D., de Cacqueray, B., Sladen, A., Roques, A., & Calbris, G. (2021). Prelim-
 485 inary assessment of ship detection and trajectory evaluation using distributed
 486 acoustic sensing on an optical fiber telecom cable. *The Journal of the Acousti-*

- 487 *cal Society of America*, 149(4), 2615–2627.
- 488 Schimmel, M., & Paulssen, H. (1997). Noise reduction and detection of weak, coherent
489 signals through phase-weighted stacks. *Geophys. J. Int.*, 130, 497–505. doi:
490 10.1111/j.1365-246X.1997.tb05664.x
- 491 Sens-Schönfelder, C., & Wegler, U. (2006). Passive image interferometry and
492 seasonal variations of seismic velocities at merapi volcano, indonesia. *Geo-*
493 *phys. Res. Lett.*, 33, L21302. Retrieved from [http://dx.doi.org/10.1029/](http://dx.doi.org/10.1029/2006GL027797)
494 [2006GL027797](http://dx.doi.org/10.1029/2006GL027797) doi: 10.1029/2006GL027797
- 495 Sheremet, A., Guza, R. T., Elgar, S., & Herbers, T. H. C. (2002). Observations
496 of nearshore infragravity waves: Seaward and shoreward propagating com-
497 ponents. *Journal of Geophysical Research: Oceans*, 107(C8), 10-1-10-10.
498 Retrieved from [https://agupubs.onlinelibrary.wiley.com/doi/abs/](https://agupubs.onlinelibrary.wiley.com/doi/abs/10.1029/2001JC000970)
499 [10.1029/2001JC000970](https://doi.org/10.1029/2001JC000970) doi: <https://doi.org/10.1029/2001JC000970>
- 500 Shinohara, M., Yamada, T., Akuhara, T., Mochizuki, K., Sakai, S., Hamakawa, M.,
501 ... Kubota, S. (2019). Distributed acoustic sensing measurement by using
502 seafloor optical fiber cable system off sanriku for seismic observation. In
503 *Oceans 2019 mts/ieee seattle* (p. 1-4). doi: 10.23919/OCEANS40490.2019
504 .8962757
- 505 Sladen, A., Rivet, D., Ampuero, J.-P., De Barros, L., Hello, Y., Calbris, G., &
506 Lamare, P. (2019). Distributed sensing of earthquakes and ocean-solid earth
507 interactions on seafloor telecom cables. *Nature Communications*, 10(1), 1–8.
- 508 Spica, Z. J., Castellanos, J. C., Viens, L., Nishida, K., Akuhara, T., Shinohara, M.,
509 & Yamada, T. (2022). Subsurface imaging with ocean-bottom distributed
510 acoustic sensing and water phases reverberations. *Geophys. Res. Lett.*, 49(2),
511 e2021GL095287. doi: <https://doi.org/10.1029/2021GL095287>
- 512 Spica, Z. J., Nishida, K., Akuhara, T., Pétrélis, F., Shinohara, M., & Yamada, T.
513 (2020). Marine sediment characterized by ocean-bottom fiber-optic seis-
514 mology. *Geophys. Res. Lett.*, 47(16), e2020GL088360. (e2020GL088360
515 10.1029/2020GL088360) doi: <https://doi.org/10.1029/2020GL088360>
- 516 Tonegawa, T., Fukao, Y., Shiobara, H., Sugioka, H., Ito, A., & Yamashita, M.
517 (2018). Excitation location and seasonal variation of transoceanic infra-
518 gravity waves observed at an absolute pressure gauge array. *Journal of*
519 *Geophysical Research: Oceans*, 123(1), 40–52. Retrieved from [https://](https://agupubs.onlinelibrary.wiley.com/doi/abs/10.1002/2017JC013488)
520 [agupubs.onlinelibrary.wiley.com/doi/abs/10.1002/2017JC013488](https://doi.org/10.1002/2017JC013488) doi:
521 <https://doi.org/10.1002/2017JC013488>
- 522 Ugalde, A., Becerril, C., Villaseñor, A., Ranero, C. R., Fernández-Ruiz, M. R.,
523 Martín-Lopez, S., ... Martins, H. F. (2021). Noise Levels and Signals Ob-
524 served on Submarine Fibers in the Canary Islands Using DAS. *Seism. Res.*
525 *Lett.*, 93(1), 351–363. Retrieved from <https://doi.org/10.1785/0220210049>
526 doi: 10.1785/0220210049
- 527 Viens, L., Bonilla, L. F., Spica, Z. J., Nishida, K., Yamada, T., & Shinohara, M.
528 (2022). Nonlinear earthquake response of marine sediments with distributed
529 acoustic sensing. *Geophysical Research Letters*, 49(21), e2022GL100122.
530 Retrieved from [https://agupubs.onlinelibrary.wiley.com/doi/abs/](https://agupubs.onlinelibrary.wiley.com/doi/abs/10.1029/2022GL100122)
531 [10.1029/2022GL100122](https://doi.org/10.1029/2022GL100122) (e2022GL100122 2022GL100122) doi: [https://](https://doi.org/10.1029/2022GL100122)
532 doi.org/10.1029/2022GL100122
- 533 Viens, L., Perton, M., Spica, Z. J., Nishida, K., Yamada, T., & Shinohara, M.
534 (2022). Understanding surface wave modal content for high-resolution imaging
535 of submarine sediments with distributed acoustic sensing. *Geophys. J. Int.*,
536 232(3), 1668–1683. Retrieved from <https://doi.org/10.1093/gji/ggac420>
537 doi: 10.1093/gji/ggac420
- 538 Williams, E. F., Fernández-Ruiz, M. R., Magalhaes, R., Vanthillo, R., Zhan, Z.,
539 González-Herráez, M., & Martins, H. F. (2019). Distributed sensing of mi-
540 croseisms and teleseisms with submarine dark fibers. *Nature communications*,
541 10(1), 1–11.

- 542 Williams, E. F., Zhan, Z., Martins, H. F., Fernández-Ruiz, M. R., Martín-López, S.,
543 González-Herráez, M., & Callies, J. (2022). Surface gravity wave interferome-
544 try and ocean current monitoring with ocean-bottom das. *Journal of Geophys-*
545 *ical Research: Oceans*, 127(5), e2021JC018375. Retrieved from [https://](https://agupubs.onlinelibrary.wiley.com/doi/abs/10.1029/2021JC018375)
546 agupubs.onlinelibrary.wiley.com/doi/abs/10.1029/2021JC018375
547 (e2021JC018375 2021JC018375) doi: <https://doi.org/10.1029/2021JC018375>
548 Xiao, H., Tanimoto, T., Spica, Z. J., Gaité, B., Ruiz-Barajas, S., Pan, M., & Viens,
549 L. (2022). Locating the precise sources of high-frequency microseisms using
550 distributed acoustic sensing. *Geophys. Res. Lett.*, 49(17), e2022GL099292.
551 (e2022GL099292 2022GL099292) doi: <https://doi.org/10.1029/2022GL099292>

Supporting Information for ”Monitoring Shelf Sea Dynamics with Ocean-Bottom Distributed Acoustic Sensing”

Loïc Viens¹ Zack J. Spica², Brent G. Delbridge¹, and Brian K. Arbic ²

¹Los Alamos National Laboratory, Los Alamos, New Mexico, USA

²Department of Earth and Environmental Sciences, University of Michigan, Ann Arbor, Michigan, USA

Contents of this file

1. Text S1 to S7
2. Figures S1 to S7

Text S1.

NDBC buoy 46229 is close to the fiber-optic cable, but a maintenance event prevented the data from being recorded between October 10 and November 14, 2021. In Figure S1, we show the wave height waveforms recorded at NDBC buoys 46229 and 46050 (locations in Figure 1). While the two buoys are located ~ 100 km from each other, their water depths are relatively similar (180 m for buoy 46229 and 160 m for buoy 46050). The wave height

waveforms are very similar as the two buoys are located above similar water depths, and we primarily use the continuous data from buoy 46050 in the main manuscript.

Text S2.

To separate the landward and oceanward propagating OSGWs, we apply a f - k filter to each 10-min time series. In Figures S2a-b, we show an example of 10-min $f - k$ filtered time series along the cable, which characterize the landward and oceanward propagating OSGWs. For each virtual source-receiver pair, we compute cross-correlation functions (CCFs) from both landward and oceanward $f - k$ filtered 10-min time windows in the frequency domain as

$$\text{CCF}_{v-r}(t) = F^{-1} \left(\frac{\hat{s}_r \hat{s}_v^*}{\{|\hat{s}_v|\}\{|\hat{s}_r|\}} \right), \quad (1)$$

where \hat{s}_v and \hat{s}_r are the Fourier transform of 10-min f - k filtered strain-rate records at the virtual source (s_v) and receiver (s_r) channels, respectively. The $*$ symbol represents the complex conjugate. The denominator of Equation 1 (i.e., $\{|\hat{s}_v|\}\{|\hat{s}_r|\}$) represents spectral whitening, where $\{\cdot\}$ is a smoothing of the absolute amplitude spectrum ($|\cdot|$) using a running-mean average algorithm over 30 discrete frequency samples (Bensen et al., 2007). The inverse Fourier transform (F^{-1}) is finally applied to retrieve the 10-min CCFs in the time domain.

Examples of CCFs computed between channel 1000 (virtual source) and all the nearby channels (receivers) are shown in Figures S2c-d. Both landward (Figure S2c) and oceanward (Figure S2d) propagating waves can be observed in the 10-min CCFs. Note that only the CCF computed between each virtual source and the 15th channel before the

virtual source is used in the main manuscript (e.g., CCF between virtual source 1000 and receiver 985).

To increase the signal-to-noise ratio, we stack the CCFs over four hours using a phase-weighted stack approach with a power of 2 and a smoothing of 0.5 s (Schimmel & Paulssen, 1997).

Text S3.

We show the correlation coefficients (CCs) after stretching along the cable for the four months of data in Figure S3a. Only the dt/t results with CCs after stretching higher than 0.4 are analyzed in the main manuscript. We illustrate the spatio-temporal dt/t data selection with a binary representation of the CCs after stretching (i.e., CC values higher and lower than 0.4) in Figure S3b. Finally, we show a histogram of the CC values in Figure S3c, which highlights that 94.4% of the CC after stretching values are above 0.4.

Text S4.

We show the bathymetry and its slope along the cable in Figure S4. The slope is computed along the array using a sliding horizontal distance of 500 m. Offshore, the largest slopes are observed between 6.3-12 km, 12-20 km, and after 40 km from the IU.

Text S5.

In the main manuscript, we focus on two regions of the cable where an oceanward surface flow is observed (i.e., dt/t values of -0.04 s). The water depths for these two regions are 79 and 206 m (i.e., 16.9 and 47.5 km from the IU). For such water depths, OSGWs with wavelengths of 158 and 412 m, or wavenumbers of 0.0063 and 0.0024 m^{-1} , respectively,

should theoretically start feeling the bottom of the ocean. In Figure S5, we show daily f - k spectra of the data at those two locations. Between 16.4 and 17.4 km from the IU (Figure S5a), the highest energy level for wind waves (i.e., above 0.1 Hz) is found for a wavenumber of 0.006 m^{-1} , which is very close to the 0.0063 m^{-1} theoretical value. Between 47 and 48 km from the IU (Figure S5b), the maximum energy, which corresponds to the swell energy, is found at a frequency of 0.06 Hz and a wavenumber of 0.002 m^{-1} , which is also very close to the theoretical wavenumber value of 0.0024 m^{-1} . This analysis shows that incoming waves with the most energy start feeling the bottom of the ocean at these two locations, which likely decreases their velocities. The shoaling of incoming waves is likely responsible for the oceanward flow of the ocean's near surface at these two locations.

Text S6.

We show the hourly wind direction and speed recorded at NDBC buoy 46050 in Figure S6. The wind is primarily coming from the North in August and September. In October and November, a clear change of the wind direction can be observed, with winds primarily blowing from the South.

Text S7.

In Figure S7, we show a comparison of the tide gauge data recorded in South Beach, OR, and the high-frequency surface current measurements near the fiber-optic cable. Rising and falling tides generally correlate with stronger landward and oceanward surface currents measured by the high-frequency radar.

References

Bensen, G. D., Ritzwoller, M. H., Barmin, M. P., Levshin, A. L., Lin, F., Moschetti,

M. P., ... Yang, Y. (2007). Processing seismic ambient noise data to obtain reliable broad-band surface wave dispersion measurements. *Geophys. J. Int.*, *169*, 1239–1260. doi: 10.1111/j.1365-246X.2007.03374.x

Schimmel, M., & Paulssen, H. (1997). Noise reduction and detection of weak, coherent signals through phase-weighted stacks. *Geophys. J. Int.*, *130*, 497-505. doi: 10.1111/j.1365-246X.1997.tb05664.x

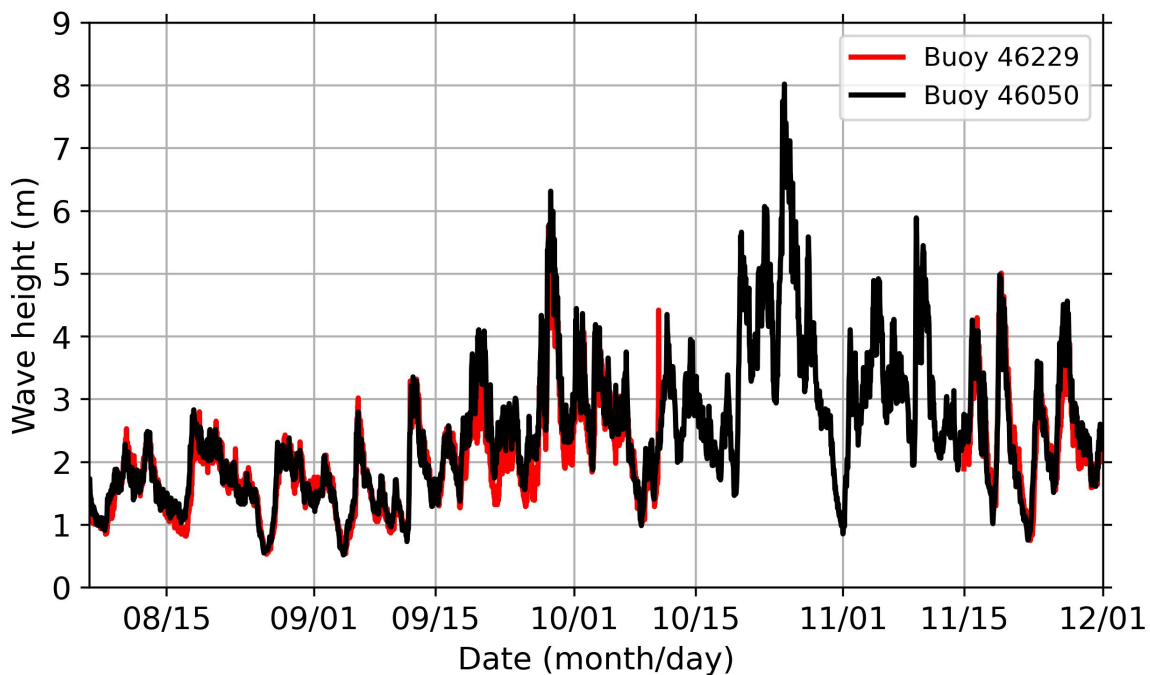


Figure S1. Comparison between the wave height recorded by buoys 46229 (red) and 46050 (black). Buoy 46229 is the closest to the cable, but has a data gap between October 10 and November 14, 2021.

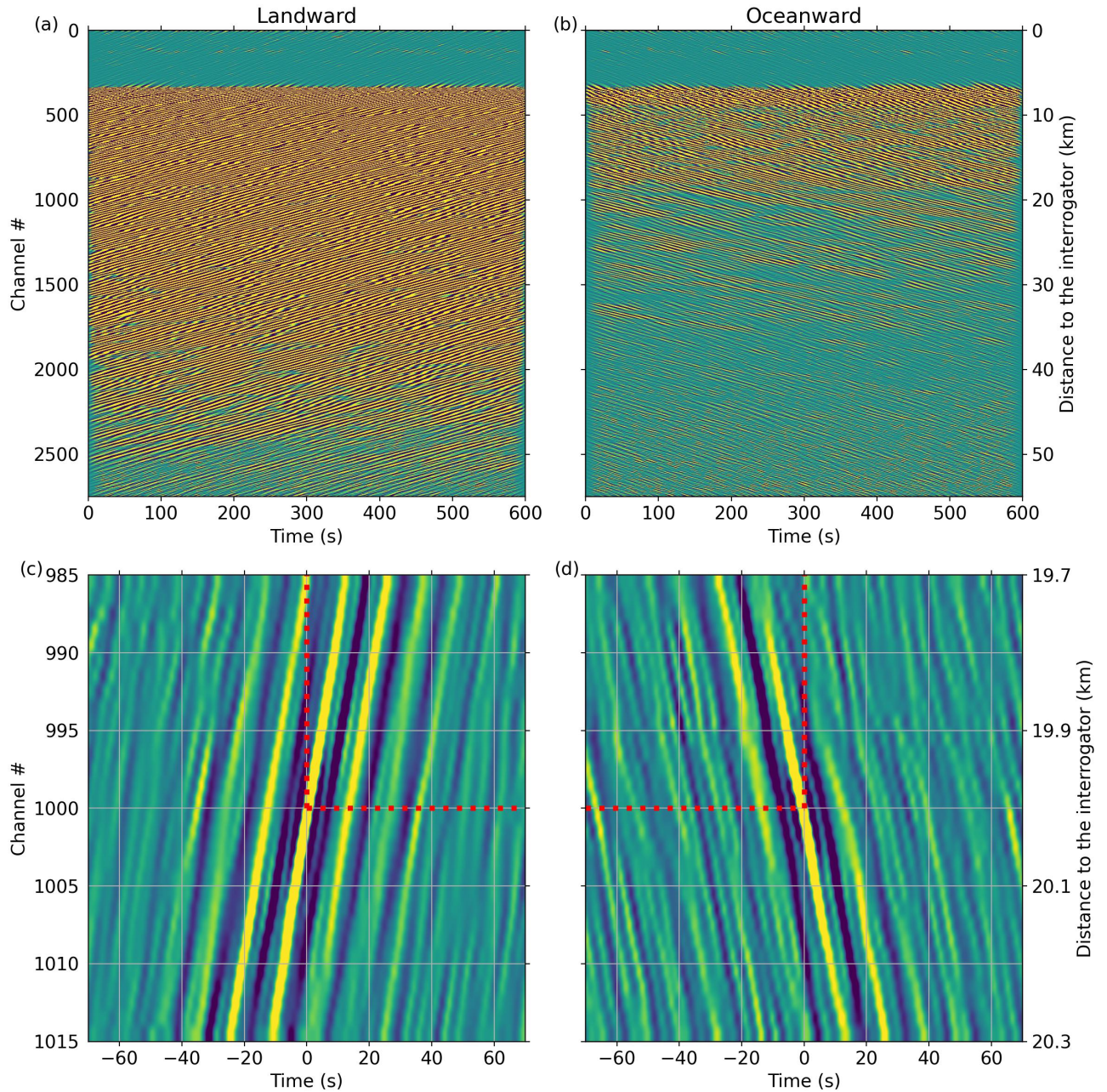


Figure S2. (a) Landward propagating OSGWs obtained after applying a $f - k$ filter to a 10-min strain-rate dataset. (b) Same as (a) for oceanward propagating waves. (c) 10-min CCFs computed using channel 1000 as the virtual source and all the nearby channels as receivers. The dashed red lines determine the quadrant representing landward propagating waves used in this study. Note that only the CCF computed between virtual source 1000 and receiver 985 is used in the analysis of the main manuscript (Chen et al., 2023). (d) Same as (c) for oceanward propagating waves.

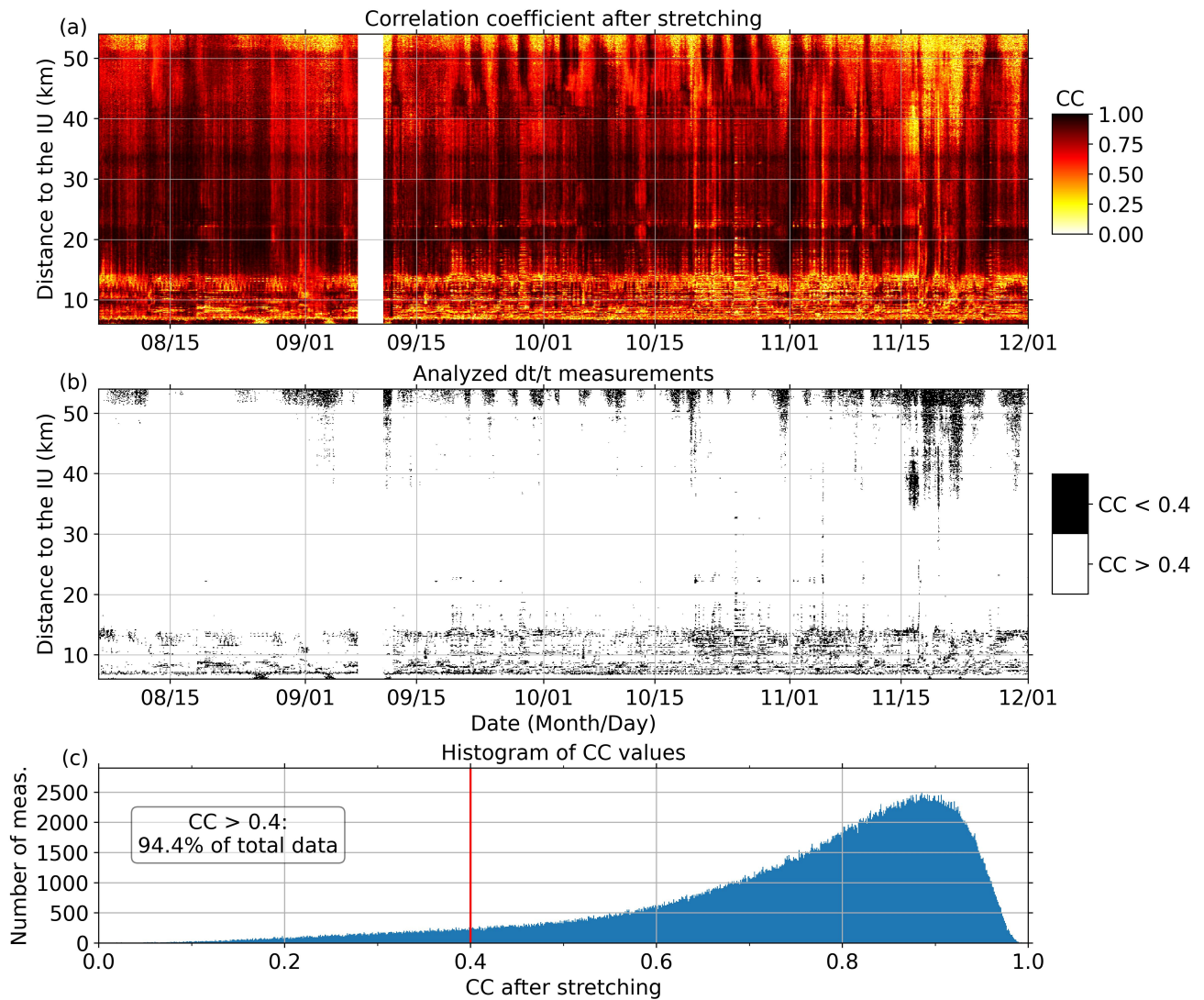


Figure S3. (a) Correlation coefficients (CCs) after stretching for the four months of data along the cable. (b) Binary representation of the selected dt/t measurements for CC after stretching values higher than 0.4. (c) Histogram of CC after stretching values. The vertical red line highlights the CC after stretching value of 0.4.

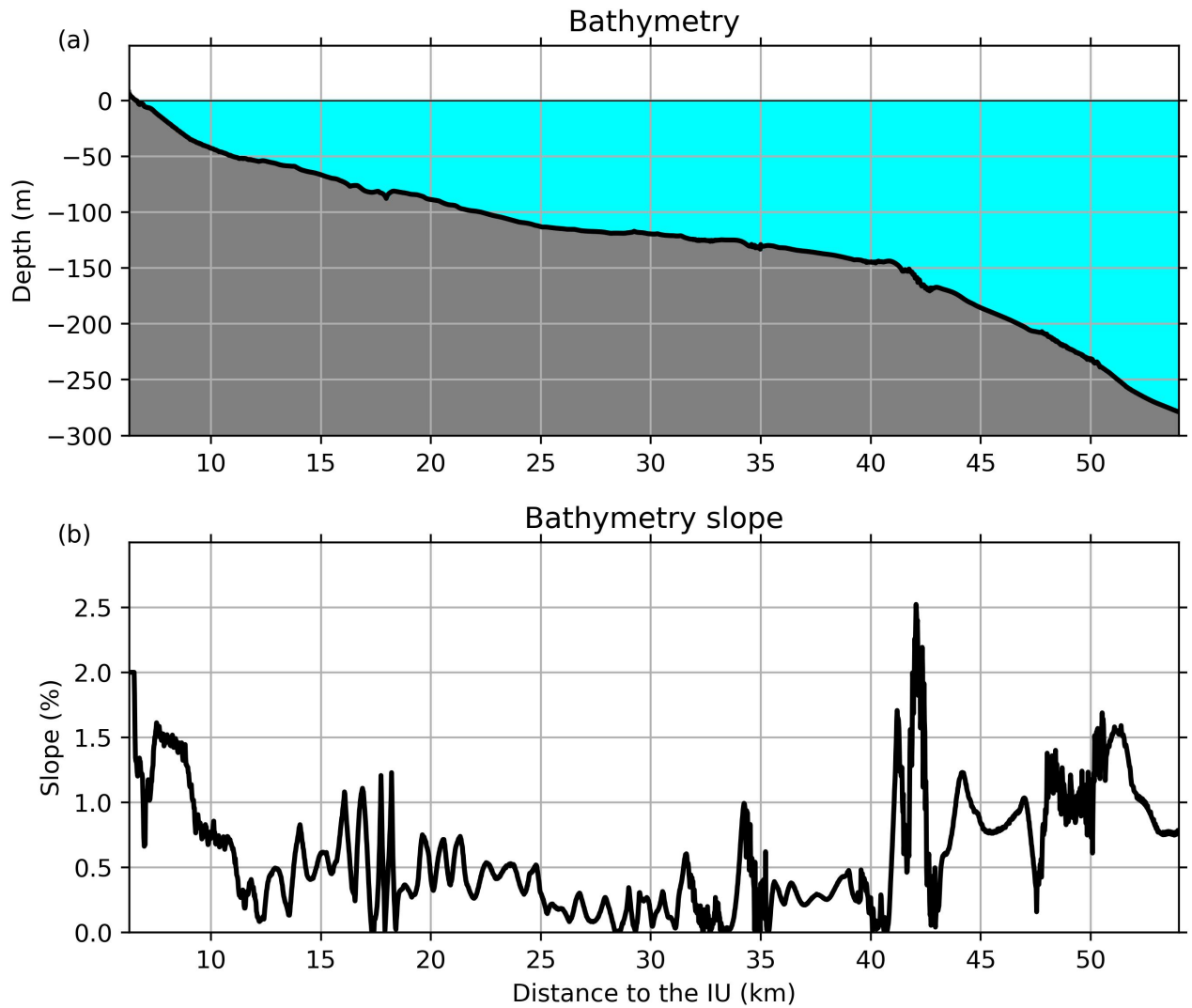


Figure S4. (a) Bathymetry profile along the cable. (b) Slope of the bathymetry profile.

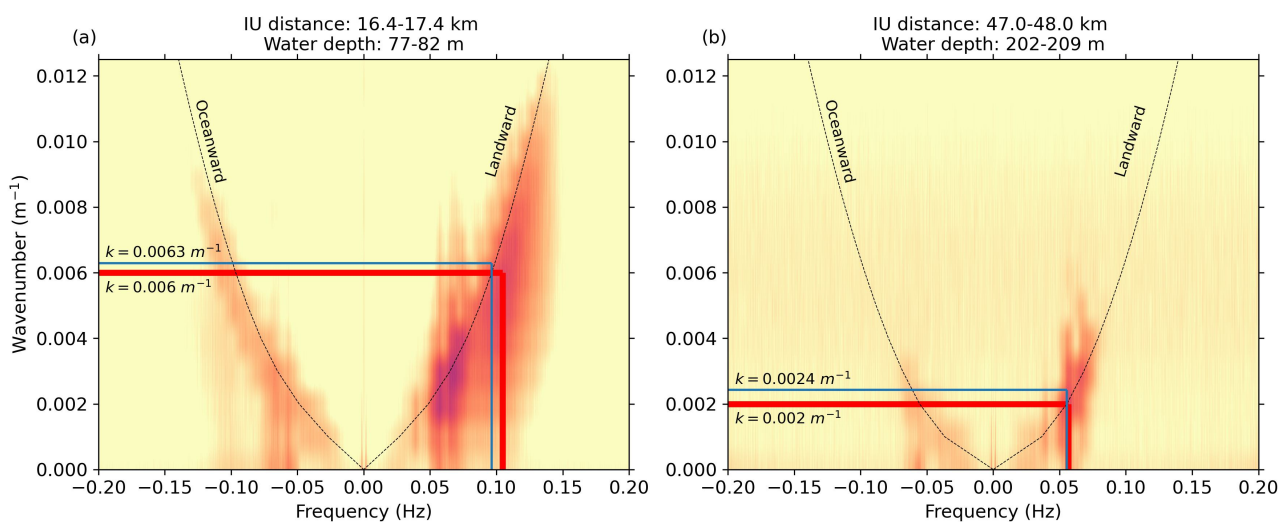


Figure S5. (a) Average f - k analysis performed between the data recorded between 16.4 and 17.4 km from the IU over one day of data. The red line highlights the frequency and wavenumber for which the maximum energy is found above 0.1 Hz. The blue line represents the theoretical wavenumber and frequency for a water depth of 79 m. (b) Same as (a) for the data recorded between 47 and 48 km from the IU and a water depth of 206 m.

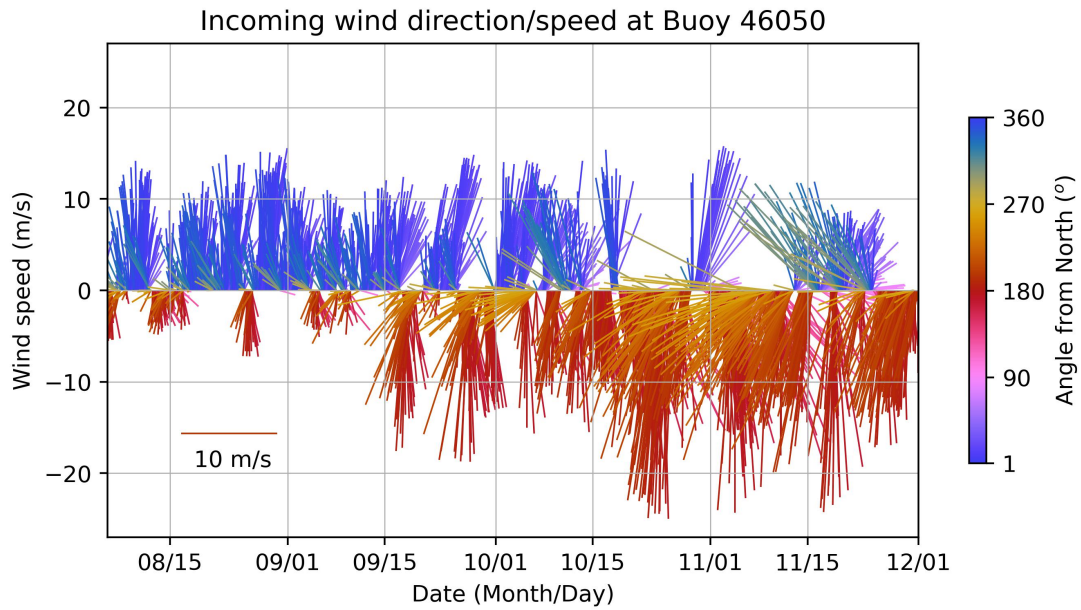


Figure S6. Hourly wind direction and speed recorded at Buoy 46050. The direction is the direction the wind is coming from in degrees clockwise from the true North, and the length of each line represents the wind speed.

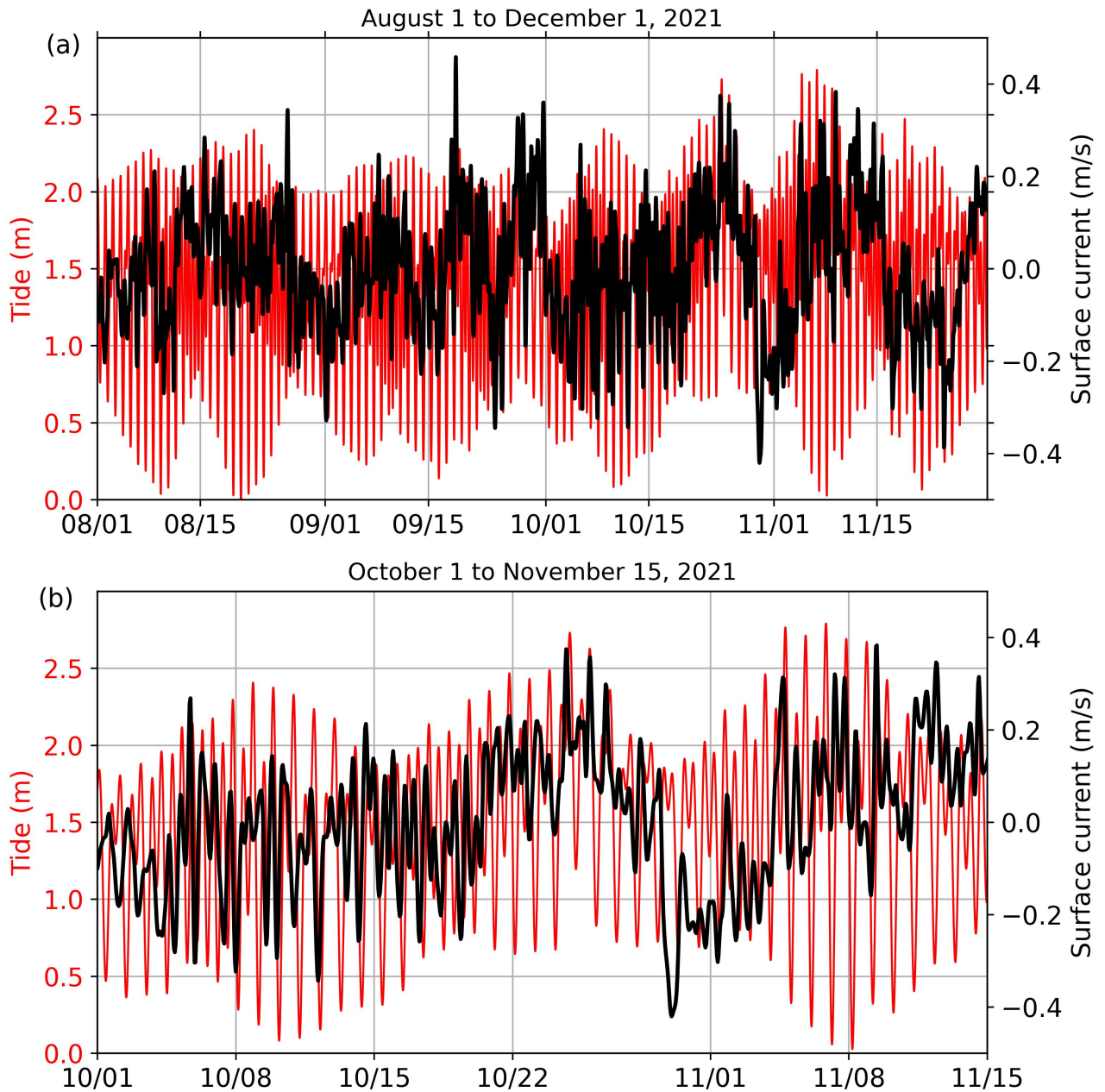


Figure S7. (a) Tide gauge (red) versus high-frequency radar east-west surface current (black) measurements between August 1 and December 1, 2021. (b) Same as (a) between October 1 and November 15, 2021.